



Determination of Precise Satellite Orbital Position Using Multi-Band GNSS Signals

Erry Gunawan
NANYANG TECHNOLOGICAL UNIVERSITY

10/16/2017
Final Report

DISTRIBUTION A: Distribution approved for public release.

Air Force Research Laboratory
AF Office Of Scientific Research (AFOSR)/ IOA
Arlington, Virginia 22203
Air Force Materiel Command

REPORT DOCUMENTATION PAGE				Form Approved OMB No. 0704-0188	
The public reporting burden for this collection of information is estimated to average 1 hour per response, including the time for reviewing instructions, searching existing data sources, gathering and maintaining the data needed, and completing and reviewing the collection of information. Send comments regarding this burden estimate or any other aspect of this collection of information, including suggestions for reducing the burden, to Department of Defense, Executive Services, Directorate (0704-0188). Respondents should be aware that notwithstanding any other provision of law, no person shall be subject to any penalty for failing to comply with a collection of information if it does not display a currently valid OMB control number.					
PLEASE DO NOT RETURN YOUR FORM TO THE ABOVE ORGANIZATION.					
1. REPORT DATE (DD-MM-YYYY) 20-12-2017		2. REPORT TYPE Final		3. DATES COVERED (From - To) 10 Sep 2015 to 09 Sep 2017	
4. TITLE AND SUBTITLE Determination of Precise Satellite Orbital Position Using Multi-Band GNSS Signals				5a. CONTRACT NUMBER 	
				5b. GRANT NUMBER FA2386-15-1-4041	
				5c. PROGRAM ELEMENT NUMBER 61102F	
				5d. PROJECT NUMBER 	
6. AUTHOR(S) Erry Gunawan				5e. TASK NUMBER 	
				5f. WORK UNIT NUMBER 	
7. PERFORMING ORGANIZATION NAME(S) AND ADDRESS(ES) NANYANG TECHNOLOGICAL UNIVERSITY 50 NANYANG AVENUE SINGAPORE, 639798 SG				8. PERFORMING ORGANIZATION REPORT NUMBER 	
9. SPONSORING/MONITORING AGENCY NAME(S) AND ADDRESS(ES) AOARD UNIT 45002 APO AP 96338-5002				10. SPONSOR/MONITOR'S ACRONYM(S) AFRL/AFOSR IOA	
				11. SPONSOR/MONITOR'S REPORT NUMBER(S) AFRL-AFOSR-JP-TR-2018-0002	
12. DISTRIBUTION/AVAILABILITY STATEMENT A DISTRIBUTION UNLIMITED: PB Public Release					
13. SUPPLEMENTARY NOTES 					
14. ABSTRACT GNSS (Global Navigation Satellite System) signals propagating through the Earth's atmosphere experience complex interactions such as scattering, refraction, and diffraction with the propagation medium. These propagation effects will highly affect the accuracy of the precise positioning using the GNSS receiver. To study these effects and avoid them, it is essential to understand well the Earth's atmosphere structure. The NTU Satellite Research Centre (SaRC) utilized a near equatorial Low Earth Orbit (LEO) satellite, VELOX-CI, to carry out radio occultation (RO) experiment. The RO data was then used to derive the ionospheric TEC profile and refractivity profile for the neutral atmosphere. It was investigated whether accurate estimation of TEC is feasible from a platform such as VELOX-CI. Of particular interest was the challenges that pervade data from LEO off-the-shelf receiver occultation platforms such as VELOX-GNSS (Global Navigation Satellite System) signals propagating through the Earth's atmosphere experience complex interactions such as scattering, refraction, and diffraction with the propagation medium. The conclusion is that accurate ionosphere profiles will generally be difficult to obtain from such data. Several reasons were identified: 1) severe cycle-slips and loss-of-lock occurring for satellites outside the main lobe of the antenna, 2) multipath on code observations making correction of carrier ambiguities difficult, especially under frequent loss-of-lock conditions, 3) poor data continuity at top of TEC profiles due to transition of satellite geometry from main lobe of side-facing antenna to zenith-facing antenna. In addition, Dr. Jade Morton (U.S.) and her team conducted mountain-based RO (MRO) experiment.					
15. SUBJECT TERMS GNSS, occultation, atmospheric, meteorological, microwave, satellite, weather					
16. SECURITY CLASSIFICATION OF:			17. LIMITATION OF ABSTRACT		18. NUMBER OF PAGES
a. REPORT Unclassified	b. ABSTRACT Unclassified	c. THIS PAGE Unclassified	SAR		16
19a. NAME OF RESPONSIBLE PERSON WINDER, SHEENA					19b. TELEPHONE NUMBER (Include area code) +81-42-511-2008

**“Determination of Precise orbital position using multi-band GNSS signals”
October 13, 2017**

Name of Principal Investigators (PI and Co-PIs):

Dr. Erry Gunawan (PI)

- e-mail address : EGUNAWAN@ntu.edu.sg
- Institution : Nanyang Technological University
- Mailing Address : School of EEE, 50 Nanyang Avenue, Singapore 639798
- Phone : (+65) 6790 5392
- Fax :

Dr. Guan Yong Liang, Co-PI

- e-mail address : EYLGUAN@NTU.EDU.SG
- Institution : Nanyang Technological University
- Mailing Address : School of EEE, 50 Nanyang Avenue, Singapore 639798
- Phone : (+65) 6790 5875
- Fax :

Dr. Yu (Jade) Morton, Co-PI

- e-mail address : jade.morton@colorado.edu
- Institution : University of Colorado Boulder
- Mailing Address : ECOT-634, Aerospace Engineering Sciences Department, University of Colorado 429 UCB, Boulder, CO 80309-0429, USA
- Phone :
- Fax :

Dr. Kay-Soon Low, Co-PI

- e-mail address : elelowks@nus.edu.sg
- Institution : National University of Singapore
- Mailing Address : Department of Electrical and Computer Engineering, National University of Singapore, Singapore 117583
- Phone : (+65) 6516 3590
- Fax :

Dr. Yung-Fu Tsai, Co-PI

- e-mail address : raymond@nspo.narl.org.tw
- Institution : National Space Organization (NSPO), Taiwan
- Mailing Address : 8F, 9 Prosperity 1st Road, Hsinchu Science Park, HsinChu , Taiwan, R.O.C.
- Phone : (+886)-3-578-4208
- Fax :

Period of Performance: September/10/2015 – September/9/2017

Abstract: GNSS (Global Navigation Satellite System) signals propagating through the Earth's atmosphere experience complex interactions such as scattering, refraction, and diffraction with the propagation medium. These propagation effects will highly affect the accuracy of the precise positioning using the GNSS receiver. To study these effects and avoid them, it is essential to understand well the Earth's atmosphere structure.

The PI's NTU Satellite Research Centre (SaRC) utilized a near equatorial Low Earth Orbit (LEO) satellite, VELOX-CI, to carry out radio occultation (RO) experiment. The RO data is then used to derive the ionospheric TEC profile and refractivity profile for the neutral atmosphere. We investigate whether accurate estimation of TEC is feasible from a platform such as VELOX-CI. Specifically, we look at the challenges that pervade data from LEO off-the-shelf receiver occultation platforms such as VELOX-

CI, and suggest the expected availability and usefulness of data. Additionally, a sparse-least-squares algorithm was developed to perform estimation of carrier ambiguities, hardware inter-frequency biases, and ionosphere TEC.

The PI's US collaborator Dr. Jade Morton and her team has conducted mountain-based RO (MRO) experiment. The collected MRO data is used to derive the atmospheric refractivity profile below the receiver's altitude and determine the planetary boundary layer (PBL)'s structure. PBL is an important layer of the lower troposphere where the Earth's surface and the free troposphere exchange energy. The PBL height (PBLH) is a crucial parameter defining the structures of PBL. We have designed algorithm that utilizes the received GNSS signals amplitude during the MRO experiment to derive the PBLH. Due to the constraint of the GNSS receiver onboard VELOX-CI, lower troposphere refractivity profile below 8km is hard to retrieve. Using the MRO data, we obtained the refractivity profiles below the receiver height, which can complement the refractivity profiles obtain from VELOX-CI.

Introduction: We aim to look at the feasibility of the VELOX-CI platform, and by extension other similar platforms, to be used for ionosphere TEC measurements. We begin with a motivation for the usefulness of VELOX-CI data. We then focus on the challenges surrounding VELOX data. Our analysis in this regard deals with the quality of observations and identifying effects that corrupt the data, such as cycle slips and multipath. We suggest how such challenges can be addressed and show some solutions. We also implement an algorithm to estimate calibrated TEC and related parameters using dual-frequency TEC measurements, which we validate and test using terrestrial data.

During the MRO experiment, unprocessed GNSS signals collected using a high-gain antenna are recorded. We want to investigate and isolate the distortions of the GNSS signals brought by the lower troposphere. The received GNSS signals contain information about the tropospheric refractivity. The received GNSS signal amplitude can be used to detect the PBLH. We apply the signal amplitude method for PBLH detection. Then, we investigate the accuracy of the signal amplitude PBLH detection method compared to the common refractivity profiles method. Besides, we implemented the open loop tracking algorithm for GPS signals scrubbing through the lower atmosphere. The better accuracy positioning determination algorithm and the GPS receiver that can be used to determine the LEO satellite's orbital position more accurately are not finished during this project period.

Experiment: In VELOX-CI satellite mission, GPS receivers are mounted on the LEO satellite to do GPS RO. The GPS receivers are commercial-off-the-shelf (COTS) receivers from Novatel. The VELOX-CI is on a near equatorial orbit with an altitude of 550km. It was launched on December 16, 2015.

A MRO experiment was conducted by the Co-PI's then team in Colorado State University (CSU) GPS Lab on April 20-26, 2015 at the summit of the Haleakala volcanic edifice on the Hawaiian island of Maui Maui (latitude: 20°42'09"N, longitude: 156°15'24"W, altitude: 3060m). The test site was chosen to have minimal obstruction and cluttering from any nearby grounds to allow the best reception of the occulting GNSS signals. During the experiment, a high-gain antenna was steered to follow rising or setting GNSS satellites in directions with no ground obstruction of the signals. The antenna is connected to a Septentrio PolaRxS PRO receiver (we shall refer to this receiver as the PolaRxS in the rest of the report) and an array of SDR. The PolaRxS generates signal amplitude, carrier phase, Doppler frequency, along with other parameters for the open GNSS signals from GPS, GLONASS, Galileo, Beidou, and QZSS. The GNSS satellites' positions and velocities are calculated from the Receiver Independent Exchange Format (RINEX) navigation files obtained from the International GNSS Service (IGS) website.

Results and Discussion:

PART I: Ionosphere TEC measurements using VELOX-CI and algorithm to estimate calibrated TEC and related parameters

Investigations were made into the use of LEO satellite TEC data for useful applications. To begin, a comparison of a well-known RO mission, COSMIC-1, was made with incoherent scatter radar measurements, as shown in Figure 1. The takeaway from the analysis is that LEO RO observations

have a large benefit in terms of vertical resolution. Further analysis of the benefit of LEO-estimated TEC rays on ionosphere imaging was also performed. Simulations of ionosphere tomography with and without LEO radio occultation-antenna and POD-antenna observations are shown in Figure 2. We demonstrate some benefit from the addition of LEO TEC rays to the ionosphere tomography problem, thus motivating further analysis of the VELOX data.

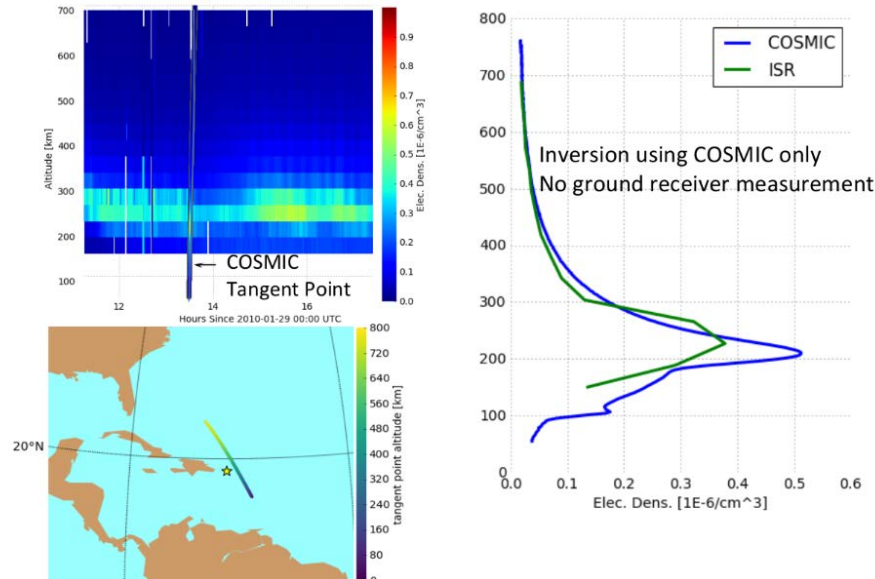


Figure 1. Benefit study comparing COSMIC radio-occultation-derived profile to nearby incoherent scatter radar estimates of ionosphere electron density. RO-derived profiles show better vertical resolution, which partly motivates the study.

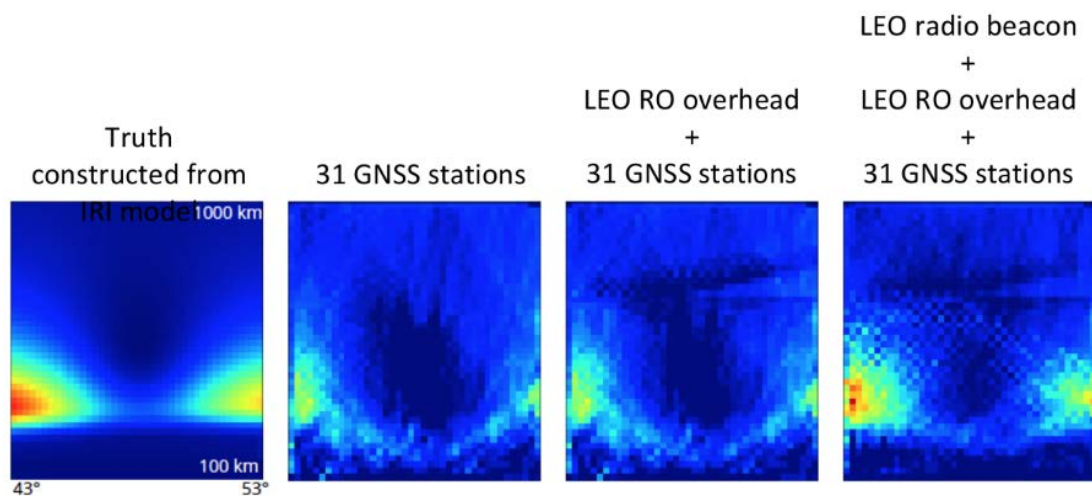


Figure 2. Benefit study of addition of radio-occultation and overhead TEC ray paths to ionosphere tomographic imaging problem. The LEO radio occultation and overhead ray paths provide some improvement in the inversion, especially at high altitudes.

Insofar as the analysis of the VELOX data, we conclude that accurate ionosphere profiles will generally be difficult to obtain from such data. We identify several reasons for this: 1) severe cycle-slips and loss-of-lock occurring for satellites outside the main lobe of the antenna, 2) multipath on code observations making correction of carrier ambiguities difficult, especially under frequent loss-of-lock conditions, 3) poor data continuity at top of TEC profiles due to transition of satellite geometry from main lobe of side-facing antenna to zenith-facing antenna.

We first address cycle-slip and loss-of-lock issues. Nominal algorithms for detecting and correcting dual-frequency GPS cycle slips were adapted to better address the VELOX data specifically. After jump detection using standard methods incorporating carrier-pseudorange difference and rate-of-

ionosphere TEC (ROT), we implemented combined polynomial fit estimation and jump correction in an algorithm designed to provide accurate estimation of relative jumps between L1/L2 carrier pseudorange differences. Figure 3 shows an example of isolated cycle slip correction.

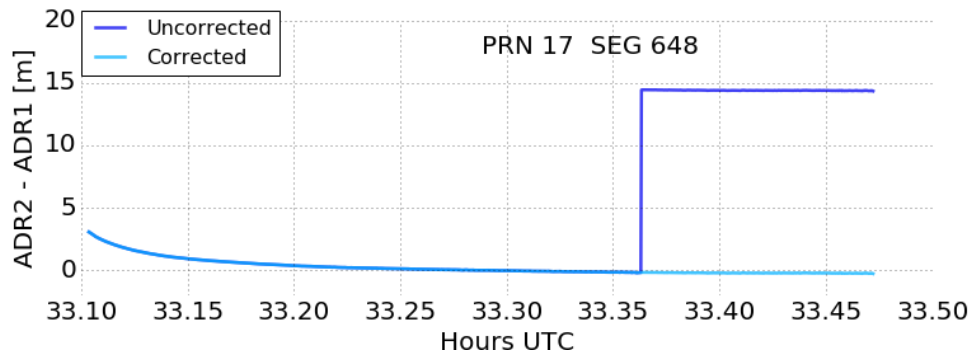


Figure 3. Shows an example of cycle slip detection and correction for PRN 17 on 2016-02-26/27. The algorithm performs multiple iterations of simultaneous polyfit and jump estimation to produce accurate relative jump magnitudes between L1/L2 carrier difference measurements.

Cycle slips / loss-of-lock can also occur in rapid succession. Figure 4 shows an example where noise in the pseudorange measurement and brevity in the duration of contiguous carrier observations causes difficulty in cycle slip correction. We conclude that such data must be ignored / thrown away, however much of the data collected by the satellite for occultation geometries shows these characteristics. More sophisticated algorithms that trade off code levelling and carrier phase continuity may be able to help.

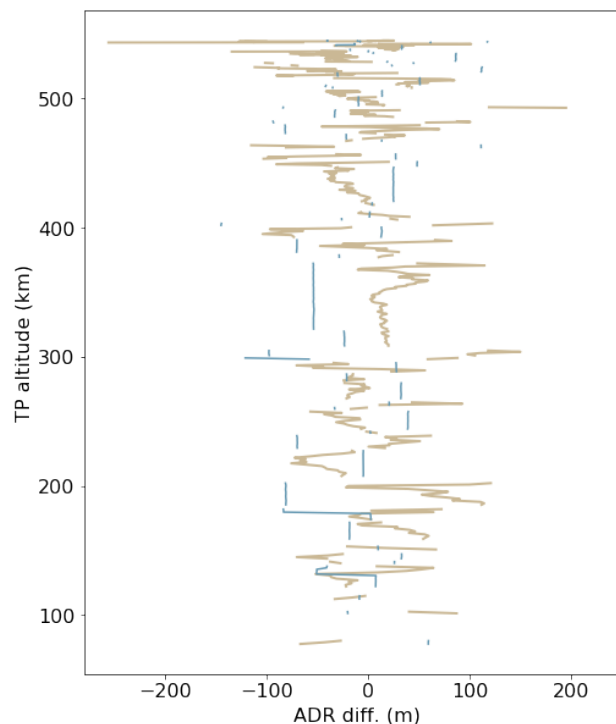


Figure 4. Shows example of cycle slips occurring in rapid succession. L1/L2 carrier pseudorange and code pseudorange differences are shown in blue and brown respectively. Loss-of-lock is evident by the dropped code measurements.

The second aspect of TEC profile retrieval difficulties pertains to multipath in the pseudorange measurement. Figure 5 shows the L1/L2 pseudorange difference, which nominally indicates ionosphere effect and multipath. A large effect can be seen in the code pseudorange differences that does not appear

in the carrier pseudorange differences. The significance of this effect is apparent when trying to use code measurements to level carrier pseudoranges. Small but impactful leveling mismatch occurs in what appears to be a quasi-systematic manner. For instance, at the beginning of each pass, the ionosphere-corrected code pseudorange difference (dark blue) appears to show overshoot/undershoot in comparison to the leveled ionosphere-corrected carrier pseudorange difference (light blue). We conclude that multipath effects of this magnitude should be prevented or modeled and corrected for future missions and use of the VELOX data for TEC estimation.

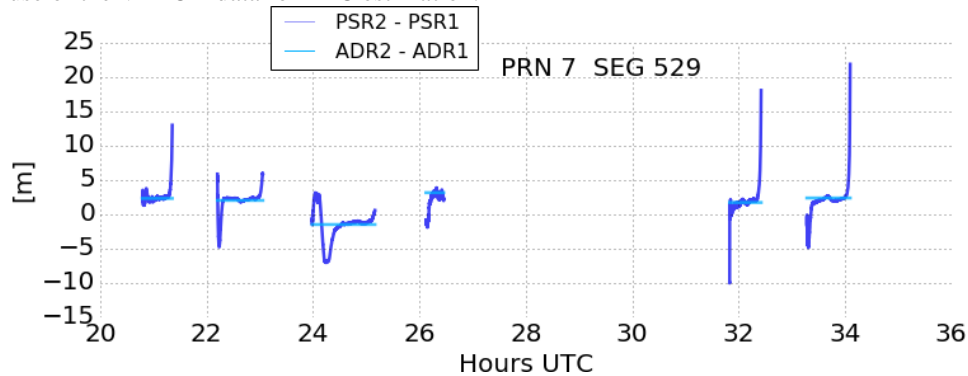


Figure 5. Leveled pseudorange differences for PRN 7. Dark blue shows ionosphere-corrected code pseudorange difference, which exhibits similar error patterns at each pass. This behavior is likely due to multipath. It can be seen for all PRNs.

The third aspect we investigate is data continuity at the top of the TEC profiles. Often, an occulting satellite would have data from a particular antenna that would become poor / corrupt toward the top of the profile. However, continuity from the top of profile to bottom profile of TEC is important in order to perform additional analysis such as topside-model fitting, etc. Figure 6 shows an example of such a profile. As such, we investigated whether it would be possible to combine measurements from different antennas to have optimal dual-frequency phase measurements that still contain the ionosphere effect, which would allow for better and more continuous TEC profiles. Figure 7 shows an analysis of the potential synergy between the antennas over the course of one orbit. We concluded that taking advantage of this synergy is possible, and should be done to improve profile retrieval.

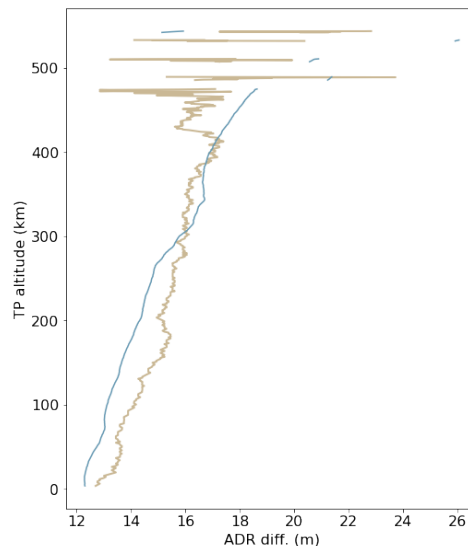


Figure 6. Example of ionosphere profile (L1/L2 diff.) showing faulty topside data due to antenna/satellite geometry. This example shows PRN 3 on 2016-02-21. Carrier pseudorange and code pseudorange differences are shown in blue and brown respectively.

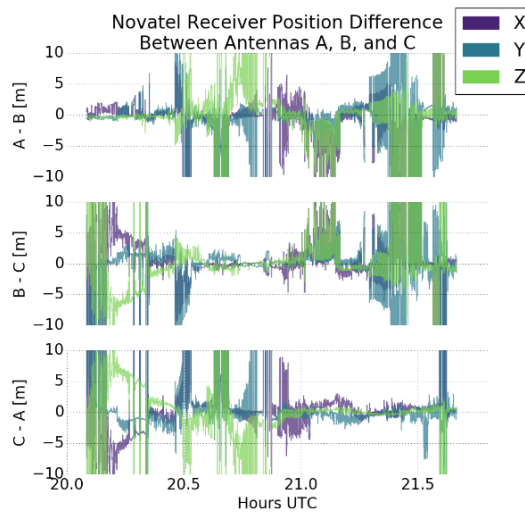


Figure 7. Receiver position difference between different antennas for 2016-01-24. The non-overlapping regions of large differences highlights the potential synergy between observations from each of the three antennas. The shift of positioning quality amongst antennas indicates the changing dilution of precision due to satellite availability that changes over the course of the orbit. When antennas have poor positioning agreement, they are likely horizon-facing and therefore have low-SNR for most antennas, but are optimally positioned to pick up occulting satellites.

With these three aspects of the VELOX-CI data classified, we determined the overall usability of the data. The altitude of available occultation data from the satellite depends on satellite orientation and time. In general, most occultations (70-90 % depending on what we count as an occultation) do not have data reaching below 100 km, but for good occultations and conditions there can be data below 40 km. The problem is that much of the data is unreliable, has large noise and multipath errors, and has frequent loss-of-lock, which means it cannot be easily-used for imaging studies since it cannot be properly calibrated. As we outlined above, we tried to address some of these challenges, but some remain outside the scope of this work.

As a final part of the work done, we implemented a sparse-linear-least-squares algorithm for computing carrier ambiguities, receiver inter-frequency biases, and TEC. The algorithm uses a 2-step approach, first estimating relative values for the desired parameters, then updating these values after applying an ionosphere model constraint using the TEC Gradient Mapping Method. The algorithm was tested and validated using terrestrial GPS data, but was designed with the purpose of ultimately working for LEO occultation datasets. This algorithm is described in a proceedings publication. In order to validate the algorithm in-orbit, the ionosphere model used to constrain the inter-frequency bias estimation will have to be adapted.

PART II: MRO experiment and PBLH detection using the MRO results.

The MRO data is used to determine the PBLH near the Hawaiian island of Maui from April 20-26, 2015. As the first time that MRO is used to detect the PBLH in subtropical region, it achieves much denser local measurements compared to co-located GNSS RO satellite remote sensing results. During the 7-day experiment, there were a total of 77 MRO events that show clear PBLH signatures.

The co-located PBLH measurements from remote sensing satellites COSMIC (Constellation Observing System for Meteorology, Ionosphere, and Climate) RO results, radiosondes from IGRA (Integrated Global Radiosonde Archive), and Cloud-Aerosol Lidar and Infrared Pathfinder Satellite Observation (CALIPSO) are used to compare and validate (latitude 17°N-23°N, longitude 160°W-155°W). Figure 8 shows the MRO GNSS receiver's location (Rcv.), MRO event locations (MRO), IGRA radiosonde station locations (HILO HI and LIHUE), the 2 COSMIC RO events' locations (COSMIC), and the CALIOP determined PBLH locations (CALIOP). An example tangent point ground track is shown for one MRO event in the figure as the dashed line. The figure shows that MRO-detected PBLH results are

much denser compared to the COSMIC events.

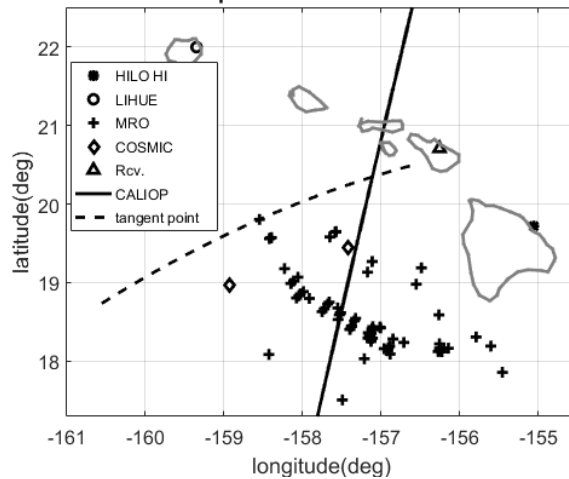


Figure 8. Relative locations where PBLH were detected using MRO (crosses), IGRA(circles), and COSMIC (diamonds) data on April 20-26, 2015 within the area defined by latitude 17°N-23°N, longitude 160°W-155°W. The CALIOP ground track containing measurements within 200km and 2 hour of the MRO data is plotted using the solid line. There are 2 COSMIC events and 77 GNSS MRO events. The triangle marks the location of the MRO receiver. The dashed line is the ground track of a MRO event.

To determine the PBLH, the common method is called the refractivity gradient method. This method calculates the vertical refractivity gradient and finds the height that corresponds to the minimum refractivity gradient. At the top of PBL, the temperature usually has a sharp increase and the water vapor has a sharp drop as altitude increases. The abrupt changes of the temperature and water vapor pressure both contribute to the decrease in refractivity as altitude increases. Therefore, the refractivity gradient can be used to detect the PBLH. The height where the minimum refractivity gradient occurs is assumed to be the top of PBL. Figure 9 shows the refractivity gradient as a function of tangent height from one radiosonde measurement at HILO HI station with a balloon released on April 24, 2015 at 12:11:07 UTC. The height where the smallest refractivity gradient occurs is marked with a star. The height is 2.3km and the refractivity gradient is -333N-unit/km. The plot shows the results for the entire measurement range while the inside inset limits to 8km in tangent height.

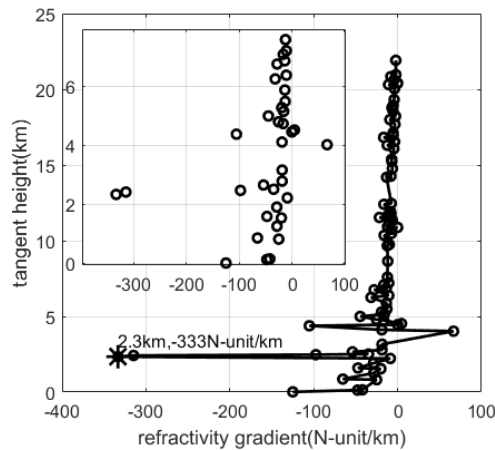


Figure 9. An example refractivity gradient profile as a function of tangent height obtained using a balloon-based radiosonde at HILO HI IGRA station released on April 24, 2015 at 12:11:07 UTC. The star marks the detected PBLH at 2.3km and with a refractivity gradient of -333N-unit/km. The inside inset is restricted to a tangent height range of 8km for better visibility.

To quantify the sharpness of the refractivity gradient, a relative minimum gradient (RMG) is adopted in this study. The RMG (N'_{rmg}) is calculated using the following equations:

$$N'_{rmg} = -(N'_{min}/N'_{rms})$$

$$N'_{rms} = \sqrt{\frac{N_1'^2 + N_2'^2 + \dots + N_m'^2}{m}}, \quad (1)$$

where m is the index for the refractivity-height profile; N' is the refractivity gradient; N'_{min} is the minimum refractivity gradient and N'_{rms} is the root mean square (RMS) value of the refractivity gradient between the threshold heights.

A new PBLH determination method, the signal amplitude method, is proposed in this project that shown to ease the detection process and obtain reliable results. This method scans the minimum signal amplitude valley, and determine the PBLH based on the geometry between the transmitter and receiver. For the MRO, GNSS signals reach the mountaintop receiver in a limb-viewing geometry. As the GNSS signals travel through the PBL, the strong refractivity gradient introduces abrupt changes in the signal's phase and Doppler, and often a drop in C/N_0 followed by a quick recovery, as shown in Figure 10. The stronger the gradient of the refractivity, the more abrupt changes in the signal's phase and Doppler frequency. The most abrupt change in refractivity gradient occurs when the signal travels through the top of the PBL. This also causes the most abrupt changes in signal carrier phase and Doppler frequency, which often results in the receiver carrier tracking loop having a difficult time maintaining lock of the signal and leads to lower C/N_0 .

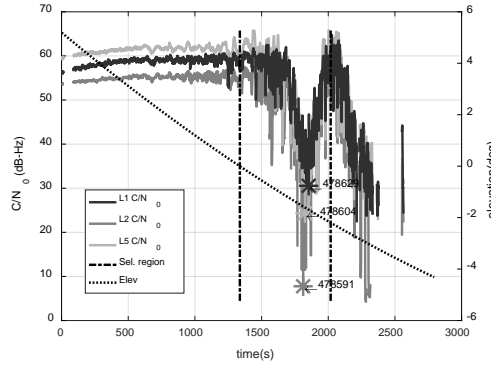


Figure 10. MRO signal C/N_0 (PolaRxS output) for GPS L1, L2 CL, and L5Q and the PBLH detected using these signals. The black dotted lines are the elevation thresholds. The stars mark the time when the lowest C/N_0 occurs. The numbers next to the stars indicate their corresponding TOWs.

Similar to the RMGs calculated in the refractivity gradient method, an amplitude relative minimum (ARM) can be defined and calculated for signal amplitude method to represent the sharpness of the PBL. A larger ARM value corresponds to a sharper amplitude. Note that the ARM values cannot be compared directly to RMGs defined earlier since they are derived from a completely different set of parameters. Similar as (1), the ARM (A_{rm}) is defined as:

$$A_{rm} = -(A_{min}/A_{rms})$$

$$A_{rms} = \sqrt{\frac{A_1^2 + A_2^2 + \dots + A_\chi^2}{\chi}}, \quad (2)$$

where χ is the index for the amplitude-time profile; A is the amplitude; A_{min} is the minimum amplitude and A_{rms} is the RMS value of the amplitude in the region.

To further validate and evaluate the performance of the signal amplitude method, the 77 MRO events

are also processed using the refractivity gradient method. the Doppler measurements generated by the PolaRxS for 67 MRO events are also used to obtain refractivity profiles and to derive the PBLHs. There are an additional 10 MRO events without positive elevation Doppler measurements. These 10 events cannot be used to derive refractivity profiles and therefore no PBLH estimations were made using refractivity gradient method, and no PBLH comparisons between the two methods. For the 67 processed events, the PBLH difference between using the signal amplitude method and the refractivity gradient method is calculated. The mean and the standard deviation of the difference are 0.09km and 0.23km, respectively. The results indicate good agreement between the two methods. Figure 11 shows the PBLH difference results with the x-axis representing the event numbers. This comparison also proves the robustness of the signal amplitude method that it does not require both positive and negative elevation measurements.

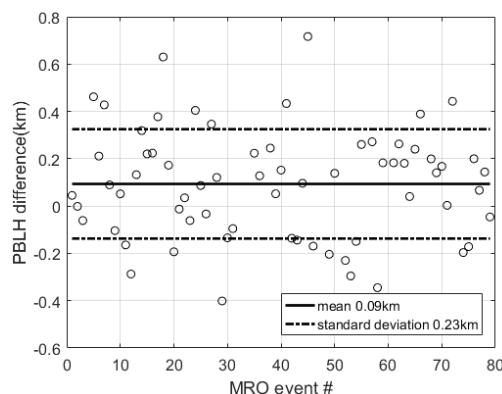


Figure 11. The PBLH differences obtained using signal amplitude method and the refractivity gradient method for 67 MRO events. The mean and standard deviation of the differences are 0.09km and 0.23km, respectively.

Figure 12 shows a map containing the PBLH results obtained from the MRO and COSMIC measurements. The values of the PBLH are color-coded according to the color bar on the right. The closely spaced events are organized into groups as outlined by the boxes. Numbers are assigned to successful PBLH detection events and are annotated in the figure. Within each group of events, the numbers are ordered from high to low latitude. The PBLH events' number, date, time, location, PBLH value, RMG for COSMIC events, ARM for MRO events, and GNSS name (GLO for GLONASS, GAL for Galileo, BDS for Beidou and QZS for QZSS) are summarized in Table I.

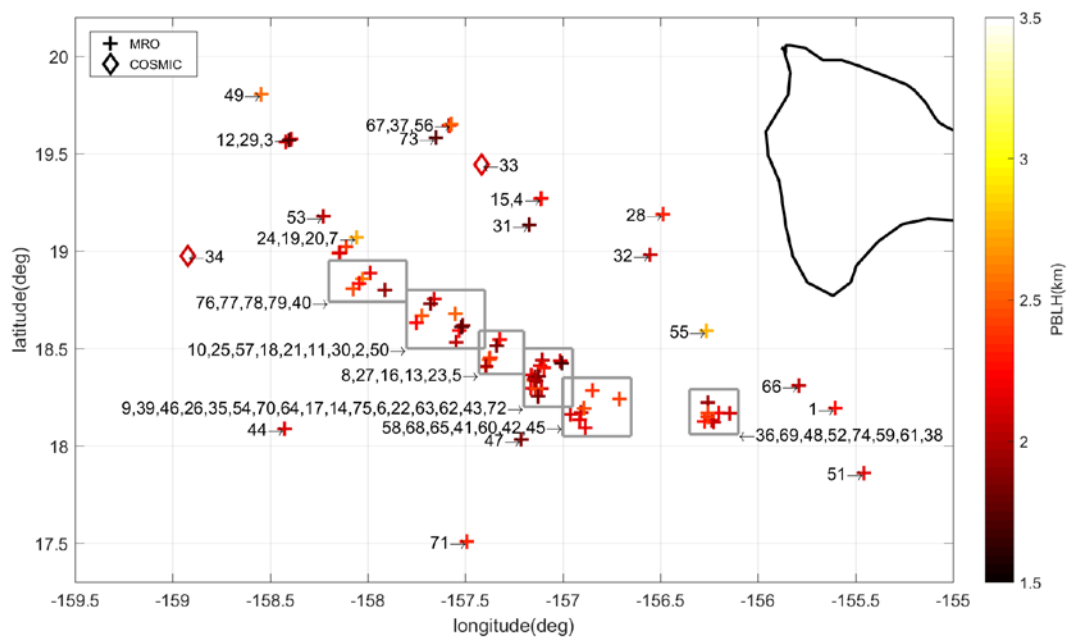


Figure 12. PBLH detection results for COSMIC and MRO measurements. A regional map is plotted with the locations of detected PBLHs marked. The diamonds indicate the COSMIC detected PBLHs, and the crosses indicate the MRO detections. The color bar shows the altitude of PBLHs. The numbers next to the markers are the event numbers, which are summarized in Table I.

Figure 13 plots the PBLH results obtained from the COSMIC, MRO, and the IGRA and the RMG and ARM values of these measurements. Note that the COSMIC and MRO measurements are not at the same location, and that RMG and ARM are based on different parameters. Except for the two balloon releases on April 26 at LIHUE station, all IGRA results have RMG values larger than 2, indicating sharp inversion layers. The IGRA detected PBLHs are more affected by the nearby terrain and are generally higher/larger compared to the PBLHs from COSMIC and MRO, and those IGRA PBLH results associated with RMG values larger than 2 are in the range of 1.7-3.4km. Due to the differences in location and time of the measurements, the MRO detected PBLHs should not be compared directly with COSMIC and IGRA data. However, the figure indicates that both the results are in the same order of magnitude.

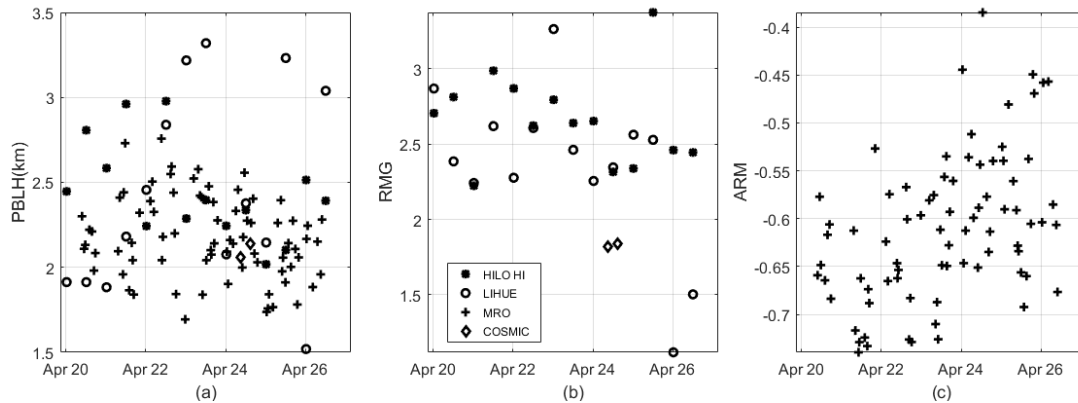


Figure 13. (a) PBLH results for “HILO HI” (solid circles), “LIHUE” (empty circles), COSMIC (diamonds), and MRO (crosses) from April 20-26, 2015; (b) corresponding RMG values for refractivity gradient method; (c) corresponding ARM values for signal amplitude method. The legend is the same for three plots and is only shown in (b).

To ensure a fair comparison with MRO results, we used CALIOP data at locations within 200km and collected within 2 hours of the MRO events. Three MRO events (#20, #21, and #60) on April 25, 2015 have corresponding CALIOP data satisfying the requirements and are used for comparison. The CALIOP level 2 cloud 1-km layer products (V4.01) are used and the cloud top altitude provided in the dataset is assumed to be the PBLH. The CALIOP PBLH results are plotted in Figure 14 and Figure 15.

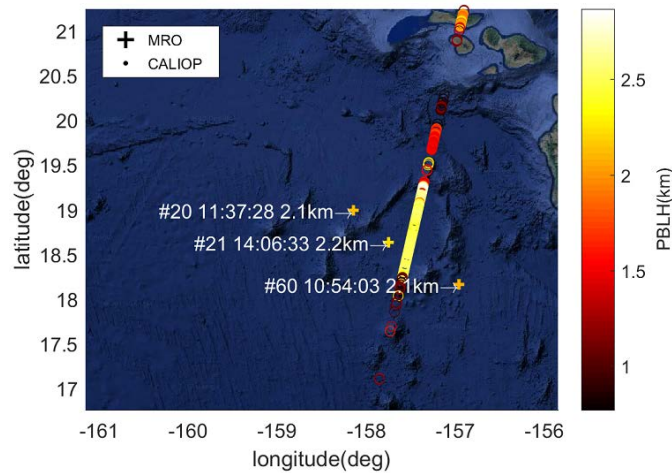


Figure 14. Comparison between the CALIOP and the MRO derived PBLH results for MRO event #20, #21, and #60. The nearly continuous ground track is the CALIOP data and the crosses are the MRO events. The results are for April 20, 2015.

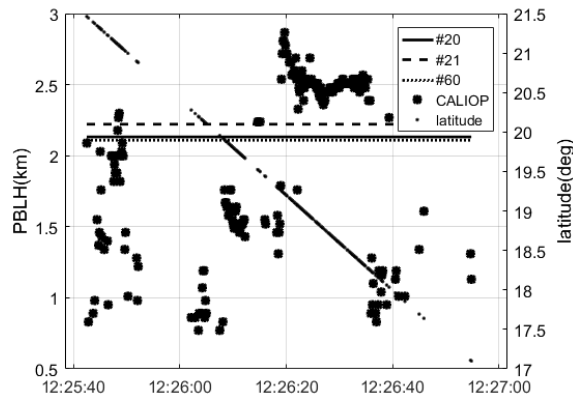


Figure 15. The CALIOP PBLH results (left y-axis) and the event latitudes (right y-axis) as functions of UTC on April 20, 2015. The three MRO events' PBLH results are also shown. Note that their values do not correspond to the time (x-axis) or latitude (right y-axis).

Figure 14 shows a regional map of the CALIOP ground track and MRO events with colors representing the PBLH values. The MRO event number, UTC, and the detected PBLH results are marked in the plot. Figure 15 shows the same results. The x-axis is the time of the measurement, and the left and right y-axes are the PBLH values and the ground track's latitude at the time of the measurement, respectively. The 3 MRO events' PBLH values are also marked as references but not plotted against neither time or latitude. The CALIOP measurements fluctuate between 0.5km and 3km while the 3 MRO events' PBLH values are between 2.1km and 2.2km. Compared to the CALIOP data point at 12:26:26 with a PBLH of 2.4km, the three nearby MRO events have slightly smaller PBLH values between 2.1km and 2.2km. The difference in the time and location could be one of the reasons causing the difference in the PBLH.

PBLH is an important parameter for climate and weather modeling. We present a technique that utilizes MRO signal amplitude measurements to derive PBLH. The method is based on detection of the occurrence of minimum signal amplitude to determine the time and value of PBLH. MRO can achieve high-resolution measurements in space and time over ocean surface using relatively low cost equipment. The signal amplitude-based PBLH detection method is simple, easy to implement, and avoids some of the assumptions and steps associated with the popular refractivity gradient-based method.

Application of the signal amplitude method to a triple-frequency GPS MRO event shows that the PBLH estimated using the three GPS signals (L1, L2 CL, L5Q) are consistent with each other with a standard deviation of 0.07km. A total of 77 GNSS MRO events were qualified for this study. The PBLH values

of these events are computed to be between 1.7km and 2.8km, well within the expected range of the PBLH in the area. The signal amplitude method is also compared with refractivity gradient method as they are both applied to measurements obtained for 67 MRO events and their mean PBLH difference is 0.09km. We introduced ARM as a measure of the sharpness of the amplitude drop. Our heuristic analysis of the measurements suggests that ARM values above 0.74 correspond to reliable estimations. The ARM values are computed for these 77 events and they fall between -0.74 and -0.38.

Three additional data sources, COSMIC, IGRA, and CALIOP are used to determine the PBLHs during the same time period around the same location of the MRO experiment. These efforts are intended to further validate the signal amplitude method and the MRO measurements.

Table I: PBLHs for MRO events #1-32, #35-79 using the signal amplitude method on all collected GNSS signals, and COSMIC events #33-34 using the refractivity gradient method. For each event, the UTC date, time, latitude (degree), longitude (degree), detected PBLH (km), corresponding RMG or ARM, and GNSS name are shown.

Event #	Date (UTC)	Time (UTC)	Lat (deg)	Lon (deg)	PBLH (km)	RMG/ ARM	GNSS name
1	4/24	12:56	18.19	-155.60	2.27	-0.38	GPS
2	4/26	01:21	18.59	-157.53	2.24	-0.46	GPS
3	4/26	00:38	19.56	-158.42	2.17	-0.60	GPS
4	4/24	19:09	19.27	-157.11	2.03	-0.54	GPS
5	4/24	16:34	18.41	-157.40	2.40	-0.63	GPS
6	4/24	15:22	18.30	-157.16	2.26	-0.58	GPS
7	4/24	11:22	18.99	-158.15	2.56	-0.54	GPS
8	4/25	16:29	18.55	-157.32	2.27	-0.54	GPS
9	4/25	15:17	18.44	-157.11	2.00	-0.66	GPS
10	4/25	13:45	18.75	-157.66	2.14	-0.69	GPS
11	4/24	01:29	18.62	-157.51	1.90	-0.65	GPS
12	4/24	00:46	19.57	-158.39	2.09	-0.44	GPS
13	4/22	16:42	18.44	-157.38	2.44	-0.73	GPS
14	4/22	15:31	18.34	-157.15	2.59	-0.60	GPS
15	4/23	19:11	19.27	-157.11	2.28	-0.56	GPS
16	4/23	16:38	18.45	-157.37	2.38	-0.63	GPS
17	4/23	15:25	18.34	-157.15	2.07	-0.65	GPS
18	4/23	13:54	18.67	-157.72	2.48	-0.56	GPS
19	4/23	11:25	19.02	-158.11	2.16	-0.61	GPS
20	4/20	11:37	18.99	-158.14	2.13	-0.65	GPS
21	4/20	14:06	18.63	-157.75	2.22	-0.66	GPS
22	4/20	15:38	18.30	-157.16	2.21	-0.62	GPS
23	4/20	16:49	18.41	-157.39	1.98	-0.61	GPS
24	4/21	11:34	19.07	-158.06	2.58	-0.66	GPS
25	4/21	14:01	18.73	-157.68	1.86	-0.72	GPS
26	4/21	15:34	18.41	-157.12	2.14	-0.73	GPS
27	4/21	16:44	18.51	-157.34	1.84	-0.69	GPS
28	4/21	20:15	19.19	-156.49	2.32	-0.53	GPS
29	4/25	00:41	19.57	-158.40	1.74	-0.53	GPS
30	4/25	01:24	18.61	-157.52	1.76	-0.54	GPS
31	4/25	19:08	19.13	-157.17	1.78	-0.45	GPS
32	4/25	20:02	18.98	-156.55	2.53	-0.47	GPS
33	4/24	14:44	19.44	-157.42	2.14	1.84	GPS
34	4/24	09:14	18.98	-158.92	2.06	1.82	GPS
35	4/26	09:57	18.40	-157.1	2.28	-0.68	GLO
36	4/26	09:12	18.22	-156.26	1.96	-0.61	GLO
37	4/26	04:26	19.64	-157.58	1.88	-0.46	BDS
38	4/24	17:20	18.12	-156.23	2.08	-0.61	GLO
39	4/25	17:56	18.44	-157.01	2.11	-0.61	GLO

40	4/25	11:59	18.80	-157.91	1.91	-0.66	GAL
41	4/25	10:31	18.17	-156.91	2.06	-0.63	GLO
42	4/24	10:33	18.14	-156.91	2.18	-0.59	GLO
43	4/24	10:04	18.29	-157.14	2.00	-0.65	GLO
44	4/24	04:28	18.09	-158.43	2.14	-0.54	GAL
45	4/24	02:40	18.09	-156.88	2.16	-0.61	GLO
46	4/22	23:44	18.42	-157.01	1.69	-0.60	GAL
47	4/22	18:11	18.03	-157.21	1.84	-0.73	GLO
48	4/22	17:25	18.17	-156.2	2.20	-0.68	GLO
49	4/22	14:56	19.80	-158.55	2.55	-0.57	GAL
50	4/22	09:43	18.53	-157.55	2.04	-0.66	BDS
51	4/23	17:11	17.86	-155.46	2.14	-0.59	BDS
52	4/23	15:04	18.17	-156.14	2.10	-0.54	GLO
53	4/23	12:25	19.18	-158.23	2.04	-0.65	BDS
54	4/22	10:17	18.36	-157.16	2.18	-0.65	GLO
55	4/22	09:23	18.59	-156.26	2.76	-0.65	GLO
56	4/22	04:51	19.64	-157.58	2.33	-0.57	BDS
57	4/22	03:56	18.68	-157.55	2.50	-0.67	GLO
58	4/22	02:46	18.28	-156.85	2.39	-0.62	GLO
59	4/20	17:40	18.13	-156.24	2.08	-0.68	GLO
60	4/20	10:54	18.16	-156.96	2.11	-0.58	GLO
61	4/20	09:39	18.13	-156.27	2.30	-0.66	GLO
62	4/21	07:23	18.29	-157.11	2.10	-0.61	BDS
63	4/21	08:21	18.29	-157.13	2.41	-0.72	GAL
64	4/21	10:17	18.35	-157.14	1.96	-0.74	GLO
65	4/21	10:44	18.19	-156.89	2.44	-0.73	GLO
66	4/21	16:07	18.31	-155.79	2.04	-0.67	GLO
67	4/23	04:48	19.65	-157.57	2.52	-0.58	BDS
68	4/23	08:37	18.24	-156.71	2.42	-0.71	GLO
69	4/23	09:28	18.17	-156.26	2.41	-0.69	GLO
70	4/23	10:09	18.36	-157.12	1.84	-0.73	GLO
71	4/24	06:11	17.51	-157.49	2.33	-0.51	GAL
72	4/25	02:06	18.25	-157.13	1.84	-0.59	GLO
73	4/25	04:28	19.58	-157.65	1.77	-0.48	BDS
74	4/25	09:13	18.15	-156.26	2.40	-0.59	GLO
75	4/25	09:59	18.34	-157.14	1.98	-0.63	GLO
76	4/26	07:14	18.89	-157.99	2.15	-0.59	QZS
77	4/24	07:26	18.81	-158.08	2.46	-0.60	QZS
78	4/23	07:32	18.86	-158.03	2.58	-0.58	QZS
79	4/25	07:21	18.83	-158.04	2.26	-0.56	QZS

List of Publications and Significant Collaborations that resulted from your AOARD supported project: In standard format showing authors, title, journal, issue, pages, and date, for each category list the following:

a) papers published in peer-reviewed journals,

None.

b) papers published in peer-reviewed conference proceedings,

None.

c) papers published in non-peer-reviewed journals and conference proceedings,

Breitsch, B., Y. Morton. "Joint estimation of ionosphere TEC, receiver inter-frequency biases, and carrier ambiguities using 3-frequency GPS measurements." URSI National Meeting, Boulder, CO, Jan. 2017.

d) conference presentations without papers,

Bo Han and Erry Gunawan. "Planetary Boundary Layer Height Detection using COSMIC Satellites," 14th Annual Meeting Asia Oceania Geosciences Society, Singapore, August 2017.

Bo Han, Erry Gunawan, Kay-Soon Low, Yu Morton, and Tieh-Yong Koh, "Performance Evaluation of Radio Occultation Data Processing Software in Southeast Asia," Joint CEDAR-GEM Workshop, New Mexico, USA, June 2016.

e) manuscripts submitted but not yet published,

Bo Han, Yu Morton, Erry Gunawan, and Dongyang Xu. "Planetary Boundary Layer Height Detection Using Mountain-based GPS Radio Occultation Signal Amplitude." submitted to IEEE Transactions on Geoscience and Remote Sensing, on January 31, 2017, re-submitted after the first review on June 14, 2017.

f) provide a list any interactions with industry or with Air Force Research Laboratory scientists or significant collaborations that resulted from this work.

During the two-year project, Mr Brian Breitsch, who is Dr. Yu Morton's student, was sponsored using the AOARD fund to study as Nanyang Technology University's Satellite Research Centre (SaRC) exchange student. He collaborated with the engineers and researcher in SaRC and investigated in the VELOX-CI ionosphere data.

Bo Han, who is Dr. Erry Gunawan's student, spend about one year in Colorado State University (CSU)'s GPS Lab as an exchange student. He attended several courses in CSU, and implemented the open loop tracking algorithm. He utilized the MRO data collected by GPS Lab and inverted the MRO data to obtain the refractivity profiles, and devised an algorithm using GNSS signal amplitude to detect the PBLH. He is currently working as a research engineer in SaRC.

This work has resulted a very close collaboration between Prof Jade Morton of Colorado University and Prof Erry Gunawan of Nanyang Technological University, Singapore.

Attachments: Publications a), b) and c) listed above if possible.

DD882: As a separate document, please complete and sign the inventions disclosure form.